ISSN 1990-3413, Astrophysical Bulletin, 2016, Vol. 71, No. 1, pp. 101–113. © Pleiades Publishing, Ltd., 2016.
Original Russian Text © N.V. Borisov, M.M. Gabdeev, V.V. Shimansky, N.A. Katysheva, A.I. Kolbin, S.Yu. Shugarov, V.P. Goranskij, 2016, published in Astrofizicheskii Byulleten, 2016, Vol. 71, No. 1, pp. 108–121.

Photometric and Spectral Studies of the Eclipsing Polar CRTS CSS 081231 J071126+440405

N. V. Borisov[1], M. M. Gabdeev[1*], V. V. Shimansky[2], N. A. Katysheva[3], A. I. Kolbin[2], S. Yu. Shugarov[3,4], and V. P. Goranskij[3]

[1] *Special Astrophysical Observatory, Russian Academy of Sciences, Nizhnii Arkhyz, 369167 Russia*
[2] *Kazan (Volga Region) Federal University, Kazan, 420008 Russia*
[3] *Sternberg Astronomical Institute, Lomonosov Moscow State University, Moscow, 119991 Russia*
[4] *Astronomical Institute of the Slovak Academy of Sciences, Tatranska Lomnica, 05960 Slovakia*

Received Dec 02, 2016; in final form, Dec 10, 2016

Abstract—We present the results of the study of the eclipsing polar CRTS CSS 081231 J071126+440405. Photometric observations allowed us to refine the orbital period of the system $P_o = 0^{\rm d}.08137673$. Considerable changes in the appearance of the object's spectra have occurred over the period of September 20–21, 2001: the slope of the continuum changed from "red" to "blue", and the variability of the line profiles over the duration of the orbital period has also changed. Doppler maps have shown a shift of the emission line-forming region along the accretion stream closer to the white dwarf. We measured the duration of the eclipse of the system and imposed constraints on the inclination angle $78.^\circ7 < i < 79.^\circ3$. The derived radial velocity amplitude was used to obtain the basic parameters of the system: $M_1 = 0.86 \pm 0.08\ M_\odot$, $M_2 = 0.18 \pm 0.02\ M_\odot$, $q = 0.21 \pm 0.01$, $R_{\rm L2} = 0.20 \pm 0.03\ R_\odot$, $A = 0.80 \pm 0.03\ R_\odot$. The spectra of the object exhibit cyclotron harmonics. Their comparison with model spectra allowed us to determine the parameters of the accretion column: $B = 31$–34 MG, $T_e = 10$–12 keV, $\theta = 80$–90°, and $\Lambda = 10^5$.

DOI: 10.1134/S1990341316010119

Keywords: *novae, cataclysmic variables — method: polarization*

1. INTRODUCTION

Cataclysmic variables are interacting close binary systems (CBS) with short orbital periods, consisting of a white dwarf (the primary component) and a late-type (K–M) red dwarf (the secondary component). The secondary component in such systems usually fills its Roche lobe and loses mass via the inner Lagrangian point L1, forming an accretion structure near the surface of the white dwarf. The nature of the accretion is determined by the strength of its magnetic field. If a highly magnetized white dwarf with a magnetic field of $B \sim 10^7$ G is present in the system, the accretion flow is controlled solely by the magnetic field, which, in turn, leads to its motion along the magnetic field lines and eventual fall onto one or two poles of the white dwarf. An accretion column is formed in the process. It is customary to refer to the group of cataclysmic variables containing highly magnetized white dwarfs as magnetic cataclysmic variables. Polars belong to this group.

The physical processes that take place in such objects manifest themselves in the entire spectral range of electromagnetic radiation. Note that despite a common set of criteria for their classification, such as, for example, very high polarization, short orbital periods, high and low states of brightness, every member of this group is individual in its observed properties [1].

A detailed study of the accretion properties plays an important role in polar research. Obviously, the rate of accretion drops significantly as the system switches from high to low state, which leads to a decrease in brightness. It is assumed that this is due to a temporary interruption in the Roche lobe overflow [2]. This gives us a chance to determine the basic physical parameters of the studied systems. Minor accretion rate variations also occur, affecting not the total brightness of the system, but rather the intensity and profiles of the emission lines. Unfortunately, the time and duration of the accretion rate changes are unpredictable, and we can only hope to be quickly notified about the results of photometric monitoring carried out by professional and amateur astronomers.

*E-mail: crucifer.troll@gmail.com

The first data on the object under study appeared on December 31, 2008, in the vsnet-alert[1] [3] service, after its outburst with an amplitude of three magnitudes. It was assigned the name CRTS CSS 081231 J071126+440405 (hereinafter CSS 081231) in the Catalina [4] sky survey catalog. Reports of deep eclipses and a short period of the system (approximately 117 min.) [5–7] were published over the following two weeks. Long-term photometric observations have shown that the object has a high orbital and long-term brightness variability, and exhibits a deep eclipse reaching $4^{\rm m}$ and a sharp dip in brightness up to $1\overset{\rm m}{.}2$ depending on the state of the system's brightness [8, 9]. V-band photopolarimetric observations of CSS 081231 in the intermediate state of brightness reported in [10] showed that the radiation in this range has a strong circular polarization; its sign changes over the orbital period. The maximum degree of polarization is reached at the moment of minimum brightness and is equal to −14polar [10].

This paper is a continuation of the program of the study of such systems [10, 11] and is dedicated to the analysis of the photometric and spectral observations of CSS 081231.

2. OBSERVATIONS AND REDUCTION

2.1. Photometry

Photometric monitoring of the object was carried out since its discovery with 5 optical instruments: the 50- and 60-cm (Zeiss-600) telescopes of the Astronomical Institute of the Slovak Academy of Sciences (AI SAS), the 125-cm ZTE and Zeiss-600 telescopes of the Crimean observatory of MSU (CO MSU), and Zeiss-1000 of SAO RAS. The information about CCD detectors used in observations one can find in Table 1. We started observing the polar on December 31, 2008, with the 50-cm telescope of AI SAS immediately after receiving notifications from the vsnet-alert service. We monitored the object until May 2009, and from December 2009 to January 2011. In 2012–2013 observations were also carried out in CO MSU and SAO RAS. The log of photometric observations can be accessed online[2].

The data on the secondary standards (Fig. 1) that were defined in the field of the object can be found in Table 2.

Observations with the 6-m telescope of SAO RAS (BTA) were carried out under good weather conditions with a seeing of about 2″. The object was observed with the SCORPIO [12] focal reducer and a liquid nitrogen-cooled EEV 42-40 (2048 × 2048) CCD camera as a detector. Using a 270 × 250-pixel array, we obtained 40 V-band frames with a 16 second time resolution in the direct imaging mode.

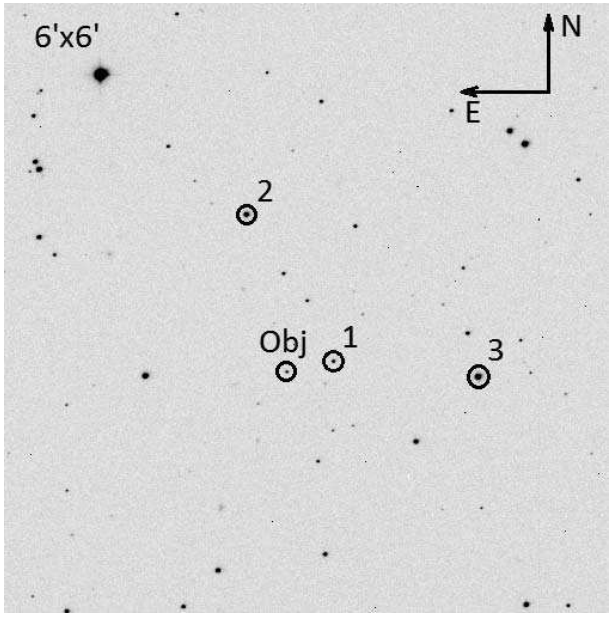

Fig. 1. Field of the object with marked secondary standards.

For the initial reduction of the photometric data we took bias and sunset sky (sunsky) frames. Dark-current frames were taken for the CCD arrays without liquid nitrogen cooling. The photometric observations were reduced using the standard methods of differential aperture photometry with the Maxim DL software.

2.2. Spectroscopy

Spectroscopic observations were performed with the 6-m BTA telescope of SAO RAS on September 20 and 21, 2011, under excellent weather conditions with a seeing of about 1″. The SCORPIO-2 [13] focal reducer was used in the "long slit" mode with a 1200 line/mm volume phase holographic grating centered at 540 nm (VPHG1200@540), and a liquid nitrogen-cooled EEV 42-90 (4600 × 2048) CCD array as a detector. Fourteen spectral images were obtained on each night in the $\lambda\lambda = 3800$–7300 Å interval with a resolution of 5.5 Å and a 300 s exposure time, covering the orbital phases $\varphi = 0.13$–0.81 (September 20, 2011) and $\varphi = 0.60$–1.29 (September 21, 2011). For further calibration during the night, we took bias, flat-field (quartz lamp), and neon (He–Ne–Ar lamp) frames, as well as the spectra of the spectrophotometric standard BD $+33^{\rm d}02642$ [14]. The observations were reduced

[1] http://ooruri.kusastro.kyoto-u.ac.jp/mailman/listinfo/vsnet-alert

[2] http://www.ta3.sk/~astrskop/j0711/PhotometryLog.pdf

Table 1. Specifications of the instruments used

Telescope	50-cm, SAS	Z-600, SAS	Z-600, CO	Z-1000, SAO	ZTE, CO	BTA, SAO
CCD	FLI ML 3041	SBIG ST10 MXE	Ap-47p	EEV 42-40	VersArray	EEV 42-40
Size, pixels	2048×2048	2174×1536	1024×1024	2048×2048	1340×1340	2048×2048
Pixel size, μ	15×15	10.9×14.8	13×13	13.5×13.5	20×20	13.5×13.5
Cooling type	Peltier	Peltier	Peltier	LN_2	LN_2	LN_2

Table 2. Data on the secondary standards

Star	Coordinates $\alpha;\delta$ (2000)	V	Rc
1	07:11:22.8; +44:04:14	16.57 ± 0.05	16.24 ± 0.03
2	07:11:28.5; +44:06:02	14.88 ± 0.01	14.45 ± 0.01
3	07:11:13.2; +44:04:03	14.01 ± 0.01	13.69 ± 0.01

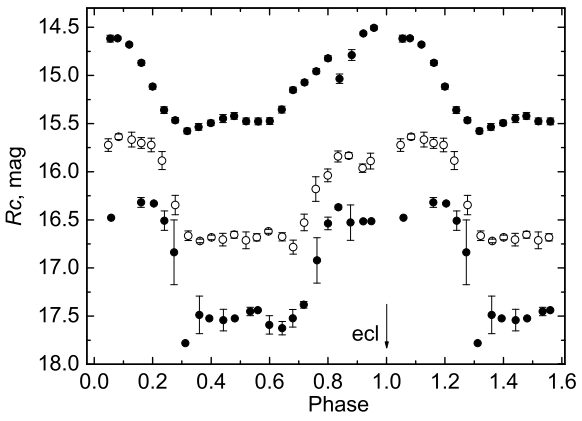

Fig. 2. R_c-band light curves of CSS 081231 in three states of brightness in apparent magnitudes. The eclipse is removed for clarity.

using standard procedures in the IDL runtime environment[3].

3. RESULTS OF PHOTOMETRIC OBSERVATIONS

Long-term photometric observations showed a strong variability of the object's brightness. The object was observed in three states: low, $R_c \sim 17\overset{\mathrm{m}}{.}5$, intermediate, $R_c \sim 16\overset{\mathrm{m}}{.}0$, and high, $R_c \sim 15\overset{\mathrm{m}}{.}0$. Fig. 2 shows the mean orbital light curves in the high, intermediate, and low states of activity. For illustrative purposes, the moments of the eclipse were removed. Evidently, the brightness increases and decreases throughout the period, which is due to the visibility of the active emitting regions. The variability amplitude is $\Delta m \sim 1\overset{\mathrm{m}}{.}0$. It does not change with the state of brightness. There is an asymmetric maximum with a short-time eclipse in the center with the depth reaching $4\overset{\mathrm{m}}{.}5$. In mid-period, $\varphi = 0.3$–0.7, the brightness of the system is practically constant. Therefore, the accretion column—the main emitting region in the continuum—is hidden behind the limb of the white dwarf. The light curve exhibits a dip at $\varphi = 0.83$–0.92, before the peak; its depth depends on the amount of matter in the stream flowing from the red dwarf. It is maximal during the high state, whereas in the low state the dip disappears altogether. Moreover, the optical depth of the stream of accreting matter can reach high values [9]. The slight increase in brightness at $\varphi = 0.48$ is apparently also due to the amount of accreting matter. The accretion structure increases in size when the accretion rate is high and is not completely hidden by the limb of the white dwarf.

It should be noted that unlike some dwarf novae, which exhibit recurrent outbursts, nova-like stars (to which polars belong) switch from low to high state of brightness spontaneously, and it is difficult to predict which state the system will be in at a given time interval. The mechanism of transfer of polars to different states of brightness remains an open question. The only part where all hypotheses agree is a change of the accretion rate.

Initially we used the ephemeris computed in the work of Thorne et al. [8]. After noticing a systematic phase shift of the eclipse position, we refined the orbital period and obtained $P_o = 0\overset{\mathrm{d}}{.}08137673(2)$, which we used from then on. A period close to ours, $P_o = 0\overset{\mathrm{d}}{.}0813768094(6)$, was reported in the paper by Schwope et al. [15].

Good weather conditions at CO MSU in November 2012 allowed us to conduct a full set of observations. Fig. 3 shows the parts of the high-state light curve covering phases 0.8 to 1.10, where the dip and the eclipse itself are clearly seen. Note the interesting shape of the eclipse—a step-like slope

[3] http://www.ittvis.com/idl

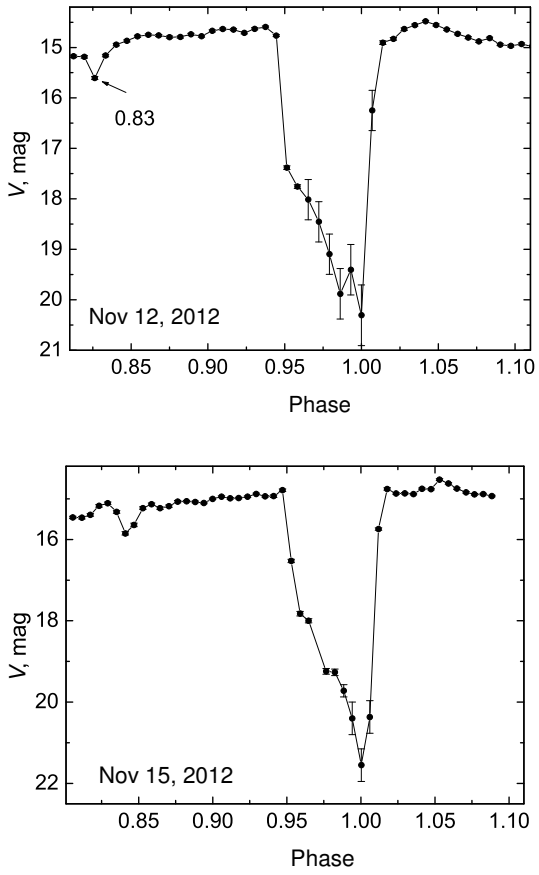

Fig. 3. V-band light curves at $\varphi = 0.8–1.1$ obtained on November 12 and 15, 2012, with the ZTE telescope of CO MSU.

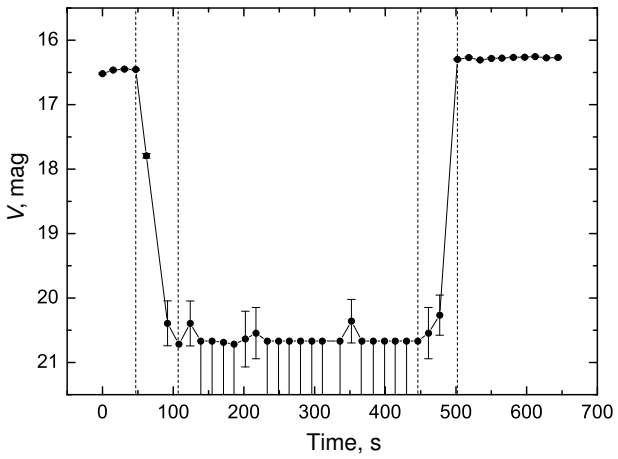

Fig. 4. Eclipse of CSS 081231 in the V-band obtained with the BTA telescope. The vertical lines show (from left to right): the start of the eclipse, the beginning of the full eclipse phase, the end of the full eclipse phase, the end of the eclipse. The upper magnitude limit is shown for the measurements with $S/N \simeq 3$.

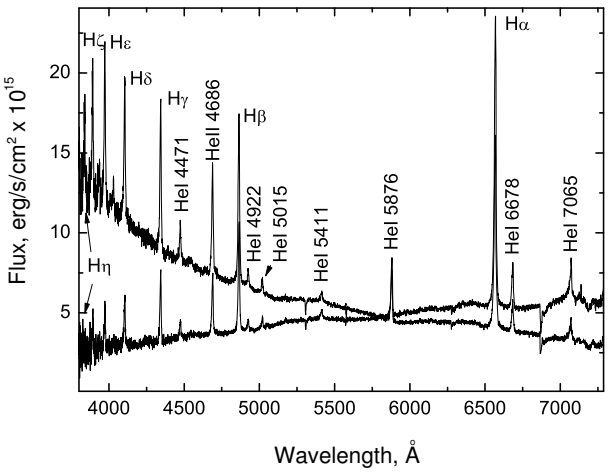

Fig. 5. Spectra of the object averaged over the phases $\varphi = 0.1–0.3$, obtained with the BTA telescope of SAO RAS on September 20 ("red" continuum) and 21 ("blue" continuum), 2011.

and an abrupt rise. Apparently, this has to do with the gradual eclipse of the continuum-emitting matter accumulated near the surface of the white dwarf.

The results of the December 5, 2012 low-state photometric observations of the eclipse conducted with the BTA telescope are shown in Fig. 4. The shape of the eclipse is different, the drop and rise of brightness are the same in duration, about 50 s, and the depth of the eclipse is about $4^{\rm m}.5$. The eclipse was in progress for about 450 s; the full phase lasted about 350 s, or 0.05 in fractions of the orbital period. During the low state of brightness, when the accretion rate is small, the accreting matter does not accumulate above the surface of the white dwarf. Therefore, the drop of brightness to minimum during the eclipse happens fast. The obtained value of the eclipse duration was used to derive the parameters of the system.

4. RESULTS OF THE SPECTROSCOPIC OBSERVATIONS

The form of the spectra of the object obtained on September 20 and 21, 2011, is typical for cataclysmic variables. Hydrogen emission lines of the Balmer series, as well as neutral and ionized helium lines, are superimposed on the continuum (Fig. 5). Evidently, the slope of the continuum changes from "red" (September 20, 2011) to "blue" (September 21, 2011) at the phases of maximum brightness $\varphi = 0.1–0.3$). The estimation of brightness from the images taken during the spectroscopic observations and with the Zeiss-1000 telescope showed that it remained the same in the V-band from September 20 to 22, 2011 (Fig. 6). Comparing the Hα line profiles at the overlapping phases $\varphi = 0.1–0.3$ (Fig. 7), we see that the lines are shifted to the red end of the

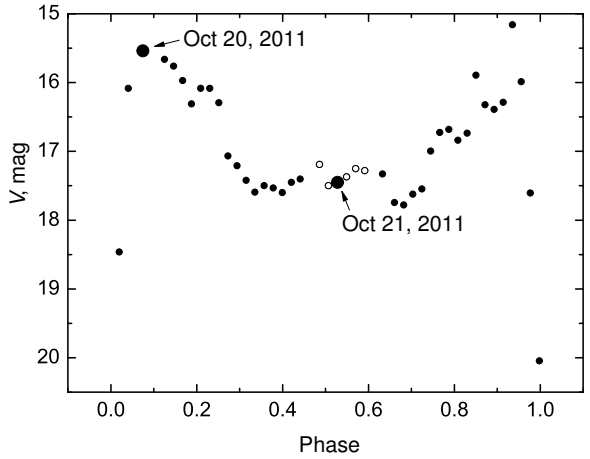

Fig. 6. The V-band light curve of the object obtained with the Zeiss-1000 telescope on September 22, 2011 (small circles). The empty circles show the brightness estimates from the September 21, 2011 data obtained with the Zeiss-1000 telescope. The large circles show the brightness estimates based on the BTA images taken immediately before the spectroscopic observations.

spectrum in the images from September 20, 2011, and that the shift of the line peaks occurs faster. The analysis of the trailed spectra, which show the variation of the intensity, profile, and Doppler shift of a line as a function of orbital phase, shows that in the September 20, 2001 observations the lines begin to split at the phases $\varphi = 0.34$–0.49; a separate peak emerges, which we do not see in the line profiles of the September 21, 2011 spectra (Fig. 8), i.e., the emission line forming region has changed over two consecutive nights. Doppler mapping has also confirmed this conclusion (see below). A distinctive feature of all the emission lines in the September 21, 2011 data is the emergence of absorption components at the phases close to the eclipse $\varphi = 0.84$–0.95 (Fig. 9). They appear in the red line wings and shift to the blue side; furthermore, the neutral helium lines become absorption lines. The He II λ4686 Å line is the exception; in this case, only the red part of the line is absorbed. This occurs due to a specific geometry of the system, where the stream of accreting matter moves in front of the red dwarf along its orbital path (as shown in Fig. 12 in [16]), and the angle of inclination of the orbit to the observer's line of sight approaches 90°. Such a peculiarity was also observed in three other polars: EF Eri [17], MN Hya [18] and FL Cet [16], manifesting itself in varying degrees and in different lines. Studying such systems is important for the research on the structure of the stream of accreting matter.

The radial-velocity measurements for the main emission lines Hα, H$_\beta$, He I λ5876 Å, He II λ4686 Å were carried out by cross-correlating them with the line in the maximum-intensity spectrum. The results corrected for the laboratory wavelength are shown in Fig. 10. A quasi-sinusoidal variation of the radial velocities takes place, with a smooth decline and a sharper rise. The radial velocities for the He II λ4686 Å line stand out due to the detected deviation from the mean value of the other lines. The velocity amplitude for the He II λ4686 Å line is noticeably higher. Comparing the available data of two nights, we conclude that the amplitude of the radial-velocity variations for Hα, H$_\beta$, He I λ5876 Å decreased on September 21, 2011. The amplitude of the velocity variations for He II λ4686 Å remains constant; sinusoidal approximation of the two data sets (from September 20 and 21, 2011) for the mentioned line shows that only the gamma velocity has changed from 230 to 80 km s^{-1} while the amplitude and zero phase remained unchanged within the errors. The value of the period was set equal to 1.

Gaussian analysis was used to measure the radial velocity of the red component of Hα at the phases $\varphi = 0.34$–0.49 in the spectra taken on September 20, 2011. We fitted two Gaussians to the obtained line profiles; the wavelength of the red peak was used to determine the velocity of the emitting matter using the well-known formula:

$$V = C \times \frac{\lambda - \lambda_0}{\lambda_0},$$

where C is the light speed, λ_0 is the laboratory wavelength, and λ is the measured wavelength. We then approximated the radial velocities of the red peak with a circular motion model; the period was set equal to one; the remaining parameters were free. As a result, the following parameters were obtained: $K_h = 334 \pm 11$ km s^{-1}, $\varphi = -0.04 \pm 0.01$, $\gamma = 61 \pm 26$ km s^{-1}. The red line component is formed at the surface of the secondary component under the influence of re-emission effects; we therefore used the value of the radial-velocity amplitude to determine the parameters of the system (see below).

5. DETERMINATION OF THE PARAMETERS OF THE SYSTEM

The available set of observational data is insufficient for an unambiguous determination of the parameters of CSS 081231. We therefore used an additional assumption that the secondary component belongs to the Main Sequence (MS) stars and has a chemical composition close to solar. This assumption is well founded since, as shown below, the white dwarf in the system has a mass of $M_1 > 0.75\,M_\odot$, i.e. is the final stage of the evolution of a star with the

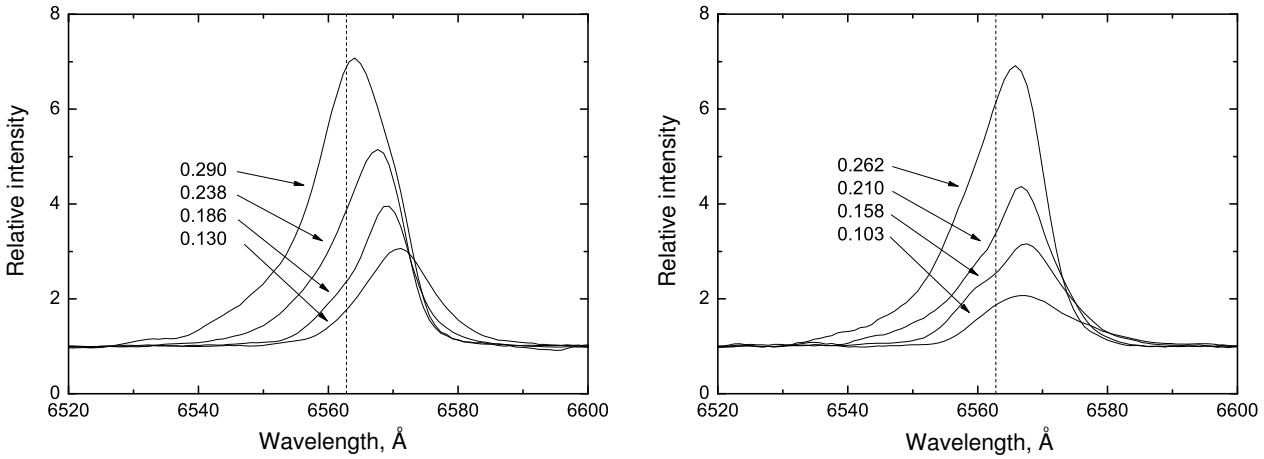

Fig. 7. Variations of the Hα line profiles at the phases $\varphi = 0.1$–0.3 on September 20, 2011 (left) and September 21, 2011 (right). The vertical line shows the laboratory wavelength of the Hα line. The numbers denote the orbital phase during which the spectrum was taken.

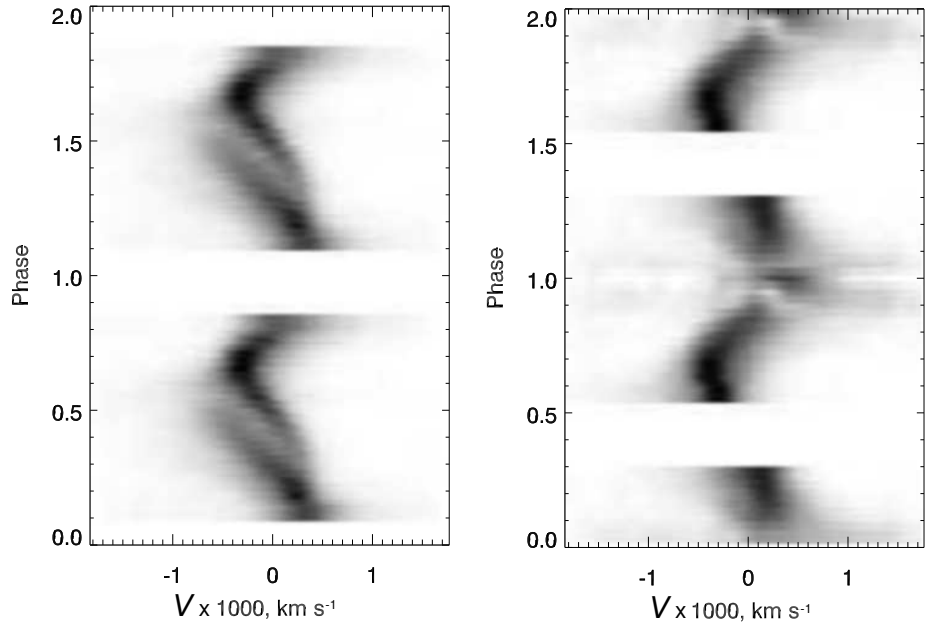

Fig. 8. Trailed spectra — the variations of the intensity, profile, and Doppler shift of a line depending on orbital phase — of Hα on September 20, 2011 (left) and September 21, 2011 (right).

initial mass of no less than 4.00 $M_\odot$ over a time of $t < 2 \times 10^9$ years. The system CSS 081231 thus belongs to the young population of the Galaxy with solar chemical composition. The secondary component could not complete its evolution at the MS stage. To determine its parameters one can use the evolutionary tracks of MS stars of different masses for $z = 0.019$ [19], which would allow one to derive the radius R_2 for a given mass. The radius of the red dwarf determined in this way was compared to the effective radius of its Roche lobe $R_{\rm L2}$, calculated for a given stellar mass ratio $q = M_2/M_1$ and major half-axis A by the formula [20]:

$$R_{\rm L} = A \times \frac{0.49\, q^{2/3}}{0.6\, q^{2/3} + \ln(1 + q^{1/3})}.$$

Note that due to the gravitational disturbance created by the white dwarf, the true radius of the secondary component is slightly bigger than the R_2 value for single MS stars. We therefore assumed that the condition $R_{\rm L2} = k \times R_{\rm L2}$ must be satisfied, where k may vary within the range of 1.03 to 1.09, i.e. the

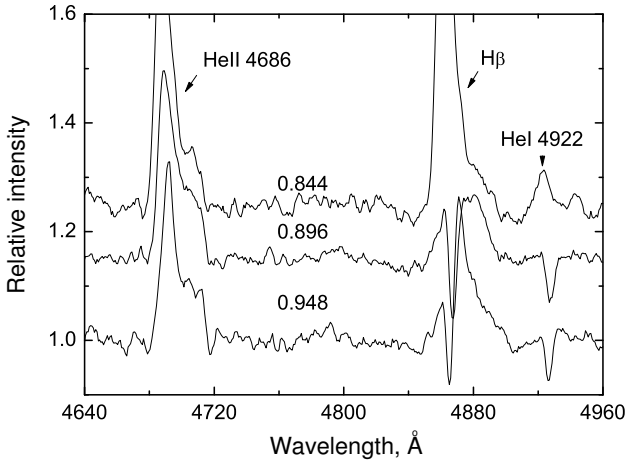

Fig. 9. Variations of the line profiles at the phases $\varphi = 0.84$–0.95 in the spectra taken on September 21, 2011.

Roche lobe radius is bigger than the evolutionary radius of the red dwarf by 3–9%.

To calculate the mass function of the white dwarf, we used the previously determined radial-velocity amplitude of the hot spot on the surface of the secondary component $K_h = 334 \pm 11$ km s^{-1}. This quantity should be corrected for the difference between the radial velocities of the star's center of mass and the hot spot ΔK_2. We determined the radial-velocity corrections on the basis of an analysis of possible line shifts in the CSS 081231 model spectra. The theoretical spectra were computed with allowance for the reflection and non-sphericity effects of the CBS components by the method developed in [21] using model atmospheres for stars with external irradiation. To conduct the computations, we specified the fundamental parameters of the secondary component (temperature, mass, radius), the components' mass ratio, and the emissive power of the X-ray source. The surface of the cool star was divided into small areas, for each of which we determined the local parameters of the stellar atmosphere ($T_{\rm eff}$, $\log g$) and external stream (inclination angle θ, ratio of the intensity of incident radiation to that of intrinsic radiation K_x). The irradiated atmosphere models for these parameters were computed by the method of plasma heating and cooling function balance developed in [22, 23]. The initial non-irradiated atmosphere models were derived using the grid interpolation [24] method described in [25]. Based on model atmospheres, we computed the synthetic spectra of every area falling within the observer's line of sight in 72 orbital phases. They were added with allowance for the influence of the star's rotation on their radial velocities and visibility conditions. The integrated spectrum of the star was shifted according to the radial velocity of its center of mass and folded with the instrument function of the spectrograph. Let us add that when modeling the spectra we took into account all the sources of non-transparency in the continuum tabulated in the SPECTR package [21], about 2 000 000 lines of atoms, ions, and sixteen basic molecules, as well as deviations from LTE for the H I, He I and He II atoms, calculated with the use of the NONLTE3 [26] software package. The chemical composition of the atmosphere of the cool star was considered to be equal to solar according to the data of [27].

The line shifts in the theoretical spectra caused by the rotation and orbital motion of the star were measured by the cross-correlation method, similar to the analysis of the observed data. The equatorial rotation velocity was assumed to be synchronous with the orbital motion and was calculated by the formula:

$$V = \frac{R \times (1+q)}{A} \times (K_h + \Delta K_2),$$

where R and V are the radius of the star and the velocity of motion for a given local area. The mutual dependence of V on the radial-velocity correction ΔK_2 made the process of their derivation iterative, with fixed values of the other parameters. In the end, we showed that for a wide range of CSS 081231 parameters, the obtained value $K_h = 334 \pm 11$ km s^{-1} determines the average equatorial rotation velocity at the level of $V = 127 \pm 3$ km s^{-1}, and the radial-velocity amplitude correction for the cool star—in the range of $\Delta K_2 = 70$–71 km s^{-1}. Test computations showed that this estimate is highly invariant to a change in the other parameters (q, K_h, A), and we set it as $\Delta K_2 = 70$ km s^{-1}. The resulting radial-velocity amplitude for the secondary component is $K_2 = 404 \pm 11$ km s^{-1}, and the mass function of the primary component is $f(M_1) = 0.56 \pm 0.04\ M_\odot$.

Further determination of the masses of the components included varying the value of q until the equality $R_{\rm L2} = k \times R_{\rm L2}$ was reached. The inclination angle of the system for a given q was calculated from the observed phase duration of the full eclipse $\Delta\varphi = 0.050$ and the results of its theoretical computations [28]. It turned out that for the acceptable (for CSS 081231) values of $q = 0.20$–0.22 the angle varies in the $i = 78\fdg7$–$79\fdg3$ range and its possible errors have no influence on the result. Finally, using the derived estimate of the mass function and the evolutionary tracks of MS stars [19], we determined the masses of both components: $M_1 = 0.86 \pm 0.08\ M_\odot$, $M_2 = 0.18 \pm 0.02\ M_\odot$ and the major half-axis $A = 0.80 \pm 0.03\ R_\odot$. The corresponding evolutionary radius of the cool star is $R_2 = 0.19 \pm 0.02\ R_\odot$, and that of its Roche lobe is $R_{\rm L2} = 0.20 \pm 0.03\ R_\odot$. Note that the main source of errors in the presented parameter

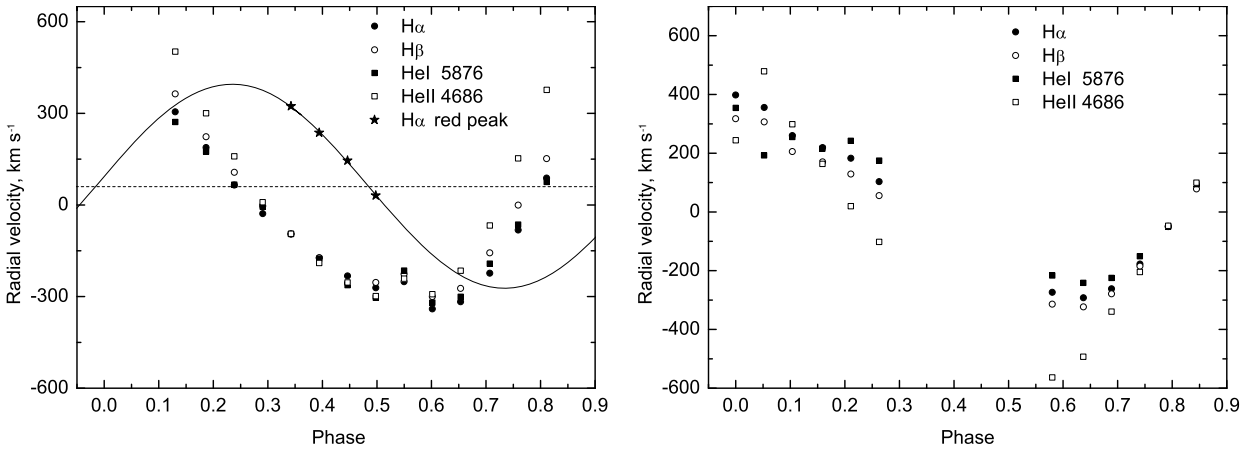

Fig. 10. Radial velocities measured from the main emission lines on September 20, 2011 (left) and September 21, 2011 (right). The stars show the radial velocities of the red component of Hα, the solid curve shows the fitted sine wave, and the dashed line shows the gamma velocity.

values is the inaccuracy of the radial-velocity amplitude K_h measurements.

The derived properties of CSS 081231 correspond, on the whole, to the most probable values for objects of this type. In particular, according to the CBS catalog [29] data, for the seventeen studied polars with the orbital periods $P_o \leq 0^{\rm d}.15$, the average mass of the primary components is $M_1 = 0.75 \pm 0.22\ M_\odot$, whereas the mass of the secondary components is $M_2 = 0.21 \pm 0.07\ M_\odot$ with the average mass ratio $q = 0.22$. We can therefore conclude that as far as fundamental parameters are concerned, CSS 081231 is a normal polar.

To verify the derived set of parameters we computed the integrated spectrum of CSS 081231 in the full-eclipse phase and compared it with the one observed. When modeling, we varied the effective temperature of the red dwarf in the $T_{\rm eff} = 3330$–3470 K range (which corresponds to the $M = 0.16$–$0.20\ M_\odot$ mass interval for MS stars) and the abundance of certain heavy elements in its atmosphere. Surface gravity was fixed at the $\log g = 5.00$ level. The best-fit criterium for the theoretical and observed spectra is the equality of their intensities in the Na I resonance doublet line blends and the TiO, MgH molecular bands in the $\lambda > 5370$ Å region.

Fig. 11 shows the resulting fit of the spectra and their residual difference, obtained with $T_{\rm eff} = 3460 \pm 20$ K, [Ti/H] = 0.2, [O/H] = [Mg/H] = [Na/H] = 0.0. The secondary component dominates in the eclipse spectrum at the wavelengths $\lambda > 5200$ Å, and its parameters correspond to a main sequence star of solar metallicity with $M = 0.20\ M_\odot$, which fully confirms the correctness of our derived CSS 081231 parameters. The emission of hot plasma is observed in the eclipse spectra in the form of hydrogen and helium emission lines, as well as the "blue" continuum in the $\lambda < 5700$ Å region. An analysis of the residual spectrum showed that it cannot be described by a Planck distribution at any plasma temperature, since the gradient $\dfrac{dF_\lambda}{d\lambda}$ is too high. The observed ratio of the eclipse duration to the orbital period indicates the formation of the continuum in the residual spectrum at a distance of $l > 0.05\ R_\odot$ from the white dwarf's surface, i.e., outside the inner region of the accretion column. Note that the point L_1 with the stream of plasma flowing towards the accretor is not observed during the eclipse. Therefore, we can conclude that the formation of the "blue" continuum in the eclipse spectrum takes place mainly in the outer layers of the accretion column, which radiate due to the effects of fluorescence. These layers also dominate in radiating emission lines, which is confirmed by their large half-width ($\Delta\lambda > 10$ Å) and a significant Doppler shift ($\delta\lambda > 4$ Å).

Estimating the extent of the visual continuum-forming region in the accretion structure of the object is of particular interest. The low duty-cycle of the photometric data for the eclipse phases allow us to estimate the duration of its individual phases at the level of $t = 51$–55 seconds (see Fig. 4) or $t = 0.0075\ P_{\rm orb}$. The corresponding size of the continuum radiating region is $l \approx 0.037\ R_\odot$. According to carbon- and oxygen-core white dwarf models [30], the radius of a star with a mass of $M = 0.86\ M_\odot$ is $R = 0.010$–$0.012\ R_\odot$, showing a certain temperature dependence. For the smallest of the possible values $M = 0.78\ M_\odot$ the maximum radius reaches $R = 0.014\ R_\odot$ at $T_{\rm eff} = 100\,000$K. Thus, the observed visual radiation-forming region is 1.4–2.0 times larger

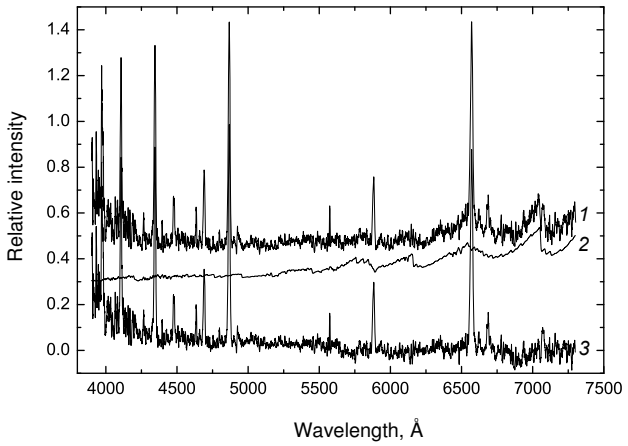

Fig. 11. The observed spectrum during the eclipse (*1*), the theoretical model of the radiation of the red dwarf, obtained for $T_{\rm eff} = 3460 \pm 20$ K, [Ti/H] = 0.2, [O/H] = [Mg/H] = [Na/H] = 0.0 (*2*), and the residual difference (*3*). For illustrative purposes, the theoretical and observed spectra are spaced along the Y-axis.

than the diameter of the white dwarf, i.e., the accretion structure becomes optically thick in the continuum at the distances of 8000–10 000 km from its physical surface.

6. DOPPLER TOMOGRAPHY

To discover the reasons for the observed differences in the spectra of CSS 081231 obtained on September 20 and 21, 2011, we used the maps of the H I, He I, and He II-line emitting areas [31] built using the Doppler tomography method. The Doppler mapping was done for the data of both nights; we used the software package written by Spruit [32], which implements the entropy minimization method, with an analysis of the observed emission lines. The maps are constructed in the velocity plane, where the x-axis points from the white dwarf towards the red dwarf, and the y-axis is directed along the orbital motion of the red dwarf. The results of Doppler mapping are shown in Figs. 12, 13, 14 and 15. In addition to the emitting regions, the maps show: the zero-velocity point, the centers of mass of both components, the Roche lobe of the red dwarf, and the Keplerian stream trajectory.

In the September 20, 2011 spectra, hydrogen line emission is formed in the re-emission region on the surface of the secondary component of the binary system and in the stream of flowing matter, which extends to the region corresponding to a velocity of $V_x = -900$ km s^{-1}, the outer boundaries of which are indistinct. Such a structure of the radiating regions manifests itself both in the Hα-line and in H$_\beta$, and is typical of the majority of polars in a relatively low state of brightness (see, e.g., [33]). The same structure of the radiating regions is also observed in He I. However, Doppler maps constructed using the line He II λ4686 Å show a totally different radiating-region structure. In this case, the maximal intensity of radiation is demonstrated by the stream of accreting matter, and the area associated with re-emission on the red dwarf's surface is practically absent. The maximum intensity peak is localized in the area corresponding to the velocity $V_x = -350$ km s^{-1}, and the structure is not very complex compared to the He I-line.

The Doppler maps constructed for the September 21, 2011 spectra differ significantly from the results of the previous night. The maximum intensity peak for the radiating areas in the H I and He I lines is shifted to the domain of greater velocities, and re-emission on the surface of the secondary component is practically absent. A low-contrast structure has formed in the region corresponding to $V_x = -500$ km s^{-1}, which is best manifested in the He I-line. The maximum intensity region for the He II λ4686 Å-line emission has increased its linear size along the stream of flowing matter by a factor of 2, whereas the position of its center in the velocity field has not changed and corresponds to $V_x = 350$ km s^{-1}.

To summarize the Doppler mapping results, we can conclude that the following features were present in the CSS 081231 system on the nights of observation:

1. The formation regions of the H I and He I emission lines differ significantly on September 20, 2011, and September 21, 2011. Whereas on the first night the main contribution to the emission in these lines was determined by the re-emission on the surface of the red dwarf, which shifted smoothly to the higher-velocity region along the flowing stream, on September 21, 2011, re-emission no longer dominated, and a low-contrast structure formed in the region corresponding to $V_x = -500$ km s^{-1}.

2. The main bright spot visible in the September 20, 2011 data in the H I and He I lines is associated with the re-emission on the surface of the secondary component, which is also confirmed by the appearance of a narrow peak in the red wing of the emission line profiles during the $\varphi = 0.34$–0.49 orbital phases. This justifies choosing the radial-velocity values determined from the red peak to find the orbital velocity of the red dwarf.

3. The maps based on the September 21, 2011 data show a moderately cool, outflowing region at $V_x = -500$ km s^{-1}, best manifested in the He I lines. It is very probable that the appearance of this additional

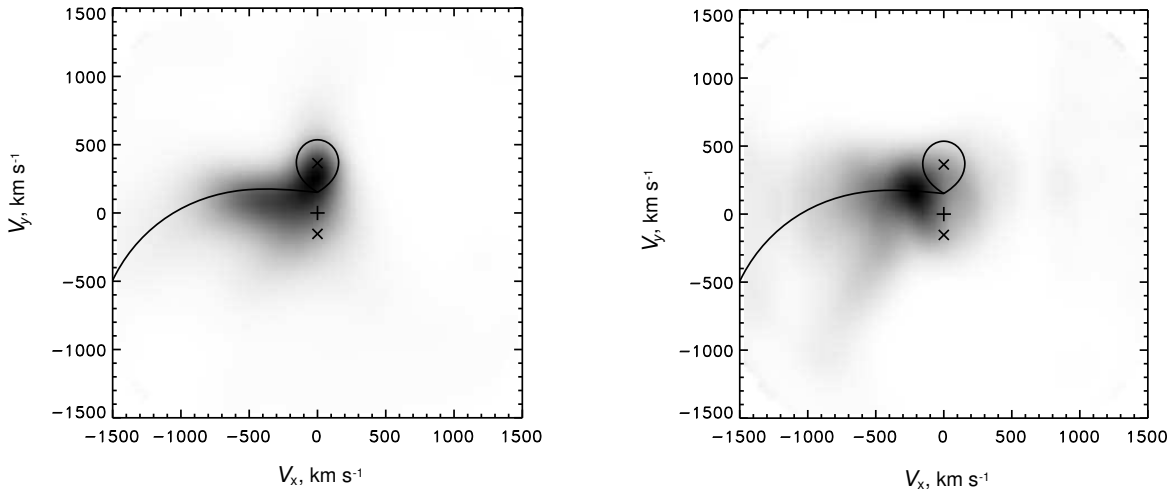

Fig. 12. Doppler maps constructed using the Hα-line from September 20, 2011 (left) and September 21, 2011 (right). The elements shown on the maps are described in the text.

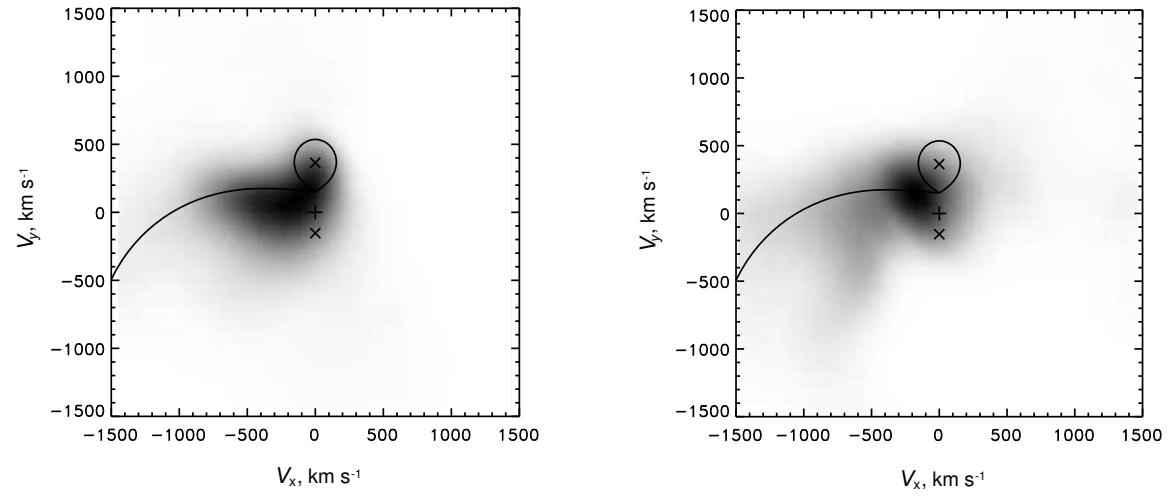

Fig. 13. Same as in Fig. 12, but for the H$_\beta$-line.

region of rarefied gas is responsible for the absorptions in the profiles of the H I, He I and He II emission lines during the $\varphi = 0.84$–0.95 orbital phases. Note that it is the neutral helium lines that become complete absorptions.

7. MODELING THE CYCLOTRON EMISSION

Modeling the cyclotron emission to determine the parameters of the accretion column was done in the assumption of thermodynamic equilibrium of the radiating medium using the HARMONY [34] code, which was used to compute the cyclotron opacity coefficients for ordinary and extraordinary waves $\alpha_\pm$. The opacity coefficients are functions of frequency ω/ω_c ($\omega_c = eB/m_e c$—cyclotron frequency), plasma temperature T_e, and the angle between the magnetic field vector and the line of sight θ. The emission intensity was computed in the assumption of a small zone of cyclotron emission and that the variations in the direction and strength of the magnetic field within this zone are small, and also that its temperature is uniform. In this case, the solution of the transfer equation for two polarization modes can be presented in the following form:

$$I_\pm = I_{\mathrm{RJ}}\big(1 - \exp(-\alpha_\pm \Lambda)\big), \qquad (1)$$

where $I_\pm$ is the intensity of ordinary and extraordinary waves, I_{RJ} is the Rayleigh-Jeans intensity, and Λ is a dimensionless parameter defined as

$$\Lambda = \frac{\omega_p^2 s}{\omega_c c}. \qquad (2)$$

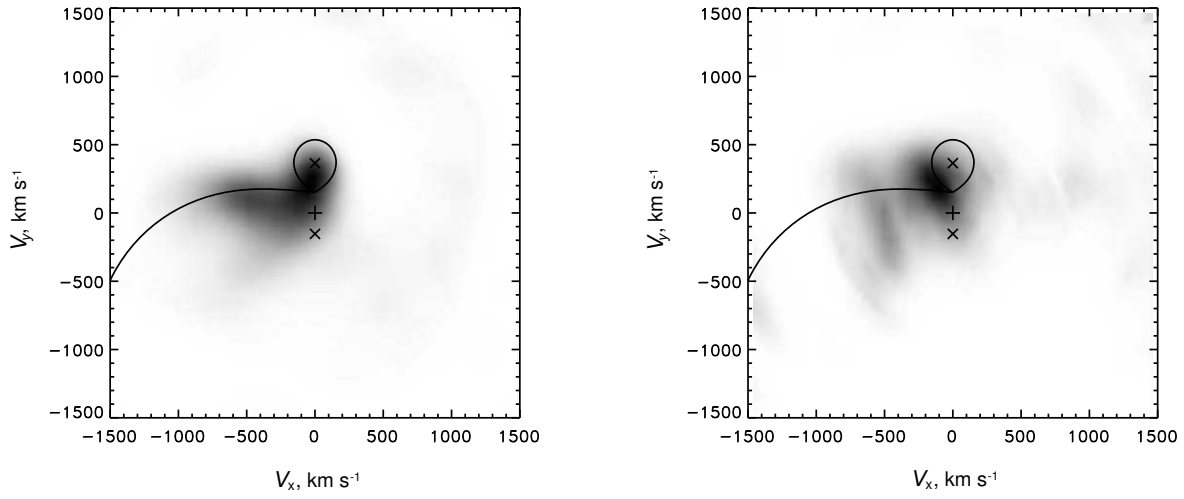

Fig. 14. Same as in Fig. 12, but for He I λ5876 Å.

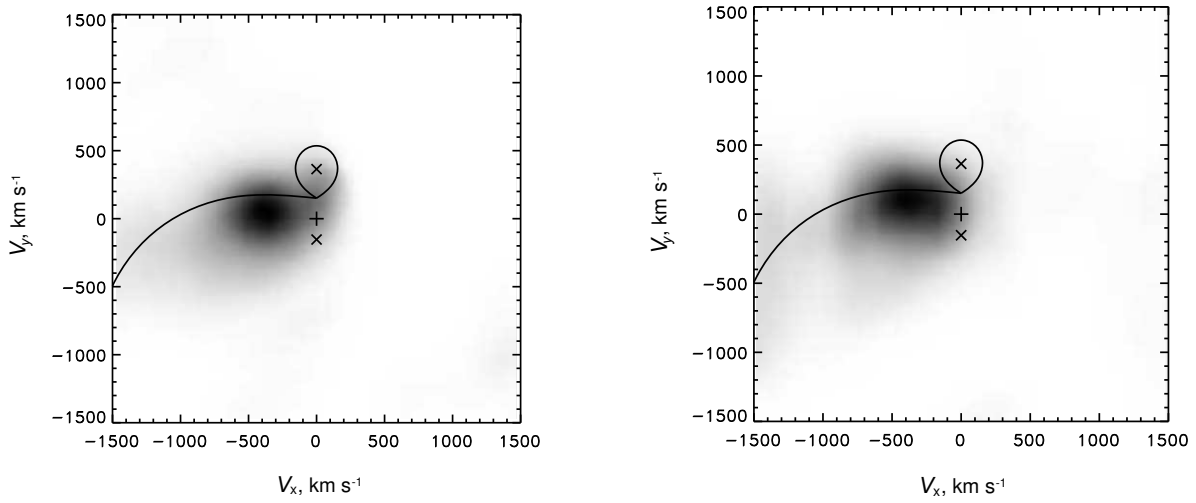

Fig. 15. Same as in Fig. 12, but for He II λ4686 Å.

The latter expression includes the geometric thickness of the emitting region along the line of sight s and the plasma frequency ω_p. The absorption coefficient in formula (1) is given in units of $\omega_p^2/\omega_c c$. The total emission intensity is determined by the sum of two polarization modes:

$$I = I_+ + I_-. \qquad (3)$$

The analysis of the spectral data for polars indicates that the zones of cyclotron emission are extended, which manifests itself in the difference between the observed spectra and the theoretical ones based on simple models [35, 36]. The analysis of photopolarimetric data also implies that the emitting regions are extended [37, 38]. Despite the existing problems with cyclotron spectra modeling, the assumption of a small cyclotron emitting zone used in this paper can be used to estimate the average parameters of the emitting region and is often employed in the analysis of modern spectroscopic data [39, 40].

We determined the physical properties of the cyclotron emission zone by comparing the theoretical and observed spectra, varying the parameters B, T_e, θ and Λ. The complex influence of these parameters on the form of the cyclotron spectrum is manifested in various effects. For example, the positions of cyclotron harmonics are sensitive to the magnetic field strength B. The temperature of the environment T_e influences the width of the harmonics, as well as the slope of the spectrum. The parameter Λ gives a similar effect. The orientation of the magnetic field vector with respect to the line of sight θ affects the sharpness of the peaks and contributes slightly to the position change of the harmonics.

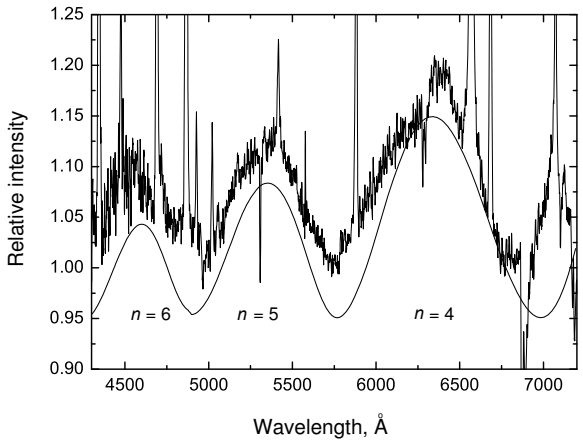

Fig. 16. Comparison of the observed and theoretical spectra of cyclotron harmonics. The numbers of the harmonics are indicated.

In the end, the best fit for the line peaks and intensities was obtained by averaging several model spectra with the following parameter ranges: $B = 31$–34 MG, $T_e = 10$–12 keV, $\theta = 80$–$90°$ and $\Lambda = 10^5$ (see Fig. 16).

CONCLUSION

The following results were obtained in the course of the investigation of the polar CSS 081231:

1. In the course of long-term monitoring, the object was observed in three states: low, $R_c \sim 17\overset{\text{m}}{.}5$, intermediate, $R_c \sim 16\overset{\text{m}}{.}0$, and high, $R_c \sim 15\overset{\text{m}}{.}0$. The transition to different states takes place without any consistent pattern. The observed peculiarities of the light curves in different states are due to the spatial size of the accretion structure, which varies depending on the accretion rate.

2. The orbital period of the system was refined, $P_o = 0\overset{\text{d}}{.}08137673(2)$.

3. The duration of the total eclipse of the system was measured and constraints were imposed on the inclination angle of the system $78\overset{\circ}{.}7 < i < 79\overset{\circ}{.}3$.

4. H I, He I, and He II emission lines are present in the spectra of the object, which are typical of cataclysmic variables. The spectral data indicate that over the period of September 20–21, 2011, changes occurred in the geometry of the emission line-forming regions and in the energy distribution in the visual spectrum of the object.

5. An analysis of Doppler maps showed that during the September 20, 2011 observations emission lines were formed mostly at the surface of the secondary component, a red dwarf, which is confirmed by the appearance of red peaks in the line profiles at the phases $\varphi = 0.34$–0.49. A day later, on September 21, 2011, this region no longer dominated; another region emerged, located near $V_x = -500$ km s^{-1} on the Doppler maps. It is quite probable that the emergence of this additional region of rarified gas is responsible for the appearance of absorption components in the profiles of the H I, He I and He II emission lines at the orbital phases $\varphi = 0.84$–0.95.

6. The following parameters of the system were derived as a result of computations: $M_1 = 0.86 \pm 0.08\ M_\odot$, $M_2 = 0.18 \pm 0.02\ M_\odot$, $R_{\text{L2}} = 0.20 \pm 0.03 R_\odot$, $A = 0.8 \pm 0.03\ R_\odot$, $q = 0.21 \pm 0.01$. A comparison of the theoretical spectrum of the red dwarf with the spectrum obtained during the eclipse confirmed the reliability of the parameter determination and the method used.

7. A comparison of the observed cyclotron emission lines with the theoretical ones allowed us to estimate the parameters of the accreting structure near the surface of the white dwarf: $B = 31$–34 MG, $T_e = 10$–12 keV, $\theta = 80°$–$90°$ and $\Lambda = 10^5$.

The given polar has an extremely unstable accretion rate, which manifests itself in its observational characteristics. We can note both the 3^{m} outburst when the object was discovered, and the variations of the light curves not only during the change of state, but also from period to period in the course of a single night. A unique phenomenon, which we were able to observe, is the change of the continuum slope and of the emission line-forming regions while the mean V-band brightness of the system remained constant. The brightness has most likely changed in the other bands as well, but, unfortunately, we do not have the data to verify this hypothesis. We can assume that polars may exhibit local variations of the accretion structure, which do not show up in single-band observations. For the detection of such phenomena, multi-band monitoring of such objects seems promising. By obtaining spectral data in different states of the system, one can thoroughly study the physics of the stream of accreting matter. Modeling the cyclotron emission will allow us to study in more detail the accretion structure that forms near the surface of the white dwarf.

ACKNOWLEDGMENTS

Observations with the 6-m BTA and Zeiss-1000 telescopes are conducted with the financial support of the Ministry of education and science of the Russian Federation (agreement No. 14.619.21.0004, project ID RFMEFI61914X0004). This work was performed with the financial support of the Russian Science Foundation (RSF 14-50-00043), and also RFBR

grants (14-02-00825, 15-42-02573, 15-02-06178 and 16-32-60039) and the grants VEGA 2/0002/13 and NSh-1675.2014.2.

REFERENCES

1. B. Warner, *Cataclysmic Variable Stars* (Cambridge Univ. Press, Cambridge, 1995).
2. M. Livio and J. E. Pringle, Astrophys. J. **427**, 956 (1994).
3. H. Maehara, vsnet-alert 10867, 2009.
4. A. J. Drake, S. G. Djorgovski, A. Mahabal, et al., Astrophys. J. **696**, 870 (2009).
5. D. Denisenko and S. Korotkiy, vsnet-alert 10870, 2009.
6. T. Kato, vsnet-alert 10874.
7. M. Templeton, A. Oksanen, D. Boyd, et al., CBET, No. 1652 (2009).
8. K. Thorne, P. Garnavich, and K. Mohrig, IBVS, No. 5923, 1 (2010).
9. N. Katysheva and S. Shugarov, Mem. Soc. Astron. Italiana **83**, 670 (2012).
10. N. V. Borisov, M. M. Gabdeev, and V. L. Afanasiev, Astrophysical Bulletin **71**, (2016).
11. M. M. Gabdeev, Astrophysical Bulletin **70**, 460 (2015).
12. V. L. Afanasiev and A. V. Moiseev, Astronomy Letters **31**, 194 (2005).
13. V. L. Afanasiev and A. V. Moiseev, Baltic Astronomy **20**, 363, (2011).
14. R. C. Bohlin, Bull. Amer. Astron. Soc., **28**, 910, (1996).
15. A. D. Schwope, F. Mackebrandt, B. D. Thinius, et al., Astronomische Nachrichten **336**, 115 (2015).
16. G. D. Schmidt, P. Szkody, L. Home, et al., Astrophys. J. **620**, 422 (2005).
17. F. Verbunt, E. P. J. van den Heuvel, T. J. van der Linden, et al., Astron. and Astrophys. **86**, 10 (1980).
18. G. Ramsay and P. J. Wheatley, Monthly Notices Royal Astron. Soc. **301**, 95 (1998).
19. L. Girardi, A. Bressan, G. Bertelli, and C. Chiosi, Astron. and Astrophys. Suppl. **141**, 371 (2000).
20. P. P. Eggleton, Astrophys. J. **268**, 368 (1983).
21. V. V. Shimanskiy, N. V. Borisov, and N. N. Shimaskaya, Astronomy Reports **47**, 763 (2003).
22. N. A. Sakhibullin and V. V. Shimanskiy, Astronomy Reports **40**, 723 (1996).
23. D. V. Ivanova, N. A. Sakhibullin, and V. V. Shimanskiy, Astronomy Reports **46**, 390 (2002).
24. R. L. Kurucz, SAO CD-Roms, (Cambridge, MA02138, 1994).
25. V. F. Suleimanov, Astronomy Letters **22**, 92 (1996).
26. N. A. Sakhibullin, Kazanskaia Gorodskaia Astronomicheskaia Observatoriia, Trudy **48**, 9 (1983).
27. E. Anders and N. Grevesse, Geochimica Cosmochimica Acta. **53**, 197 (1989).
28. K. Horne, Monthly Notices Royal Astron. Soc. **213**, 129 (1985).
29. H. Ritter and U. Kolb, Astron. and Astrophys. **404**, 301 (2003).
30. J. A. Panei, L. G. Althaus, and O. G. Benvenuto, Astron. and Astrophys. **353**, 970 (2000).
31. T. R. Marsh, Monthly Notices Royal Astron. Soc. **231**, 1117 (1988).
32. H. C. Spruit, arXiv:astro-ph/9806141 (1998).
33. A. Schwope, K.-H. Mantel, and K. Horne, Astron. and Astrophys. **319**, 894 (1997).
34. R. Mahadevan, R. Narayan, and I. Yi, Astrophys. J. **465**, 327 (1996).
35. A. D. Schwope, K. Beuermann, and H.-C. Thomas, Astron. and Astrophys. **230**, 120 (1990).
36. D. T. Wickramasinghe and L. Ferrario, Astrophys. J. **334**, 412 (1988).
37. M. Cropper and K. Horne, Monthly Notices Royal Astron. Soc. **267**, 481 (1994).
38. S. B. Potter, M. Cropper, and P. J. Hakala, Monthly Notices Royal Astron. Soc. **315**, 423 (2000).
39. R. K. Campbell, T. Harrison, A. D. Schwope, and S. B. Howell, Astrophys. J. **672**, 531 (2008).
40. G. H. Tovmassian, P. Szkody, J. Greiner, et al., Astron. and Astrophys. **379**, 199 (2001).

Translated by E. Chmyreva